

Superconducting qubit as a quantum transformer routing entanglement between a microscopic quantum memory and a macroscopic resonator

Alexander Kemp,^{1,*} Shiro Saito,¹ William J. Munro,^{1,2} Kae Nemoto,² and Kouichi Semba^{1,†}

¹*NTT Basic Research Laboratories, NTT Corporation, 3-1 Morinosato Wakamiya Atsugi-shi, Kanagawa 243-0198, Japan*

²*National Institute of Informatics 2-1-2 Hitotsubashi, Chiyoda ku, Tokyo 101-8430, Japan*

(Received 6 July 2011; published 8 September 2011)

We demonstrate experimentally the creation and measurement of an entangled state between a microscopic two-level system (TLS), formed by a defect in an oxide layer, and a macroscopic superconducting resonator, where their indirect interaction is mediated by an artificial atom, a superconducting persistent current qubit (PCQB). Under appropriate conditions, we found the coherence time of the TLS, the resonator, and the entangled state of these two are significantly longer than the Ramsey dephasing time of PCQB itself. This demonstrates that a PCQB can be used as a quantum transformer to address high coherence microscopic quantum memories by connecting them to macroscopic quantum buses.

DOI: [10.1103/PhysRevB.84.104505](https://doi.org/10.1103/PhysRevB.84.104505)

PACS number(s): 03.67.Lx, 03.75.Lm, 85.25.Cp

I. INTRODUCTION

The twentieth century saw the discovery of one of the most fundamental and far reaching theories ever developed, quantum mechanics. Quantum mechanics provides a set of principles describing physical reality at the atomic level of nature and is critical to our understanding of how atomic devices work. It has important implications for the processing of information at this atomic level and in fact allows for a paradigm shift to quantum information processing. Quantum mechanics provides a fundamentally different computational model by employing features not present in a classical world, most notably, superposition and entanglement. Such coherence properties, however, are not restricted to the microscopic world. Quantum coherence in macroscopic objects has been observed in a number of physical systems, which are usually referred to as macroscopic quantum coherence effects. These effects can be most prominent in solid-state systems such as engineered superconducting electronic systems.¹ We can now design quantum circuits on a controllable scale, making quantum mechanics available as a technological resource. As an example, circuit quantum electrodynamics experiments²⁻⁴ have demonstrated the coupling of artificial two-level systems (qubits) to single photons in macroscopic superconducting resonators. Other researchers have demonstrated^{5,6} the use of such resonators as versatile quantum buses⁷⁻⁹ to couple distant qubits, leading to experimental demonstrations of quantum algorithms¹⁰ and Bell violations.¹¹ In the longer term, with the promising developments in highly integrated nanotechnologies, these are going to be important to construct superconducting quantum information processors. However, imperfections and defects will degrade the performance of such devices. One particular defect of recent interest are microscopic two-level systems (TLSs) inside the barriers of Josephson junctions. These are individual quantum objects,¹²⁻¹⁷ usually acting as an decoherence source, however, they can also be used as proxies for engineered qubits¹⁸ for experimentally testing quantum operations. Their properties, particularly their limited controllability and coherence time, typically longer than superconducting qubits, makes them behave as passive quantum memories.¹⁹ This leads to the natural task to access and manipulate the TLSs' state, and

entangle them with other quantum systems. We demonstrate how to do this for the case of a macroscopic resonator, even if these objects do not directly couple strongly to one another. In this paper, we use resonant interactions of a superconducting persistent current qubit (PCQB) with either system to mediate the entanglement.

II. THE SYSTEM

We begin with an overview of the sample layout, schematics, and micrograph of the PCQB, resonator, and TLS, depicted in Fig. 1.²⁰ The central element [Fig. 1(b)] is the PCQB (Ref. 21) in a four Josephson junction configuration,²² placed directly on the substrate. The electric scheme in Fig. 1(c) contains the PCQB loop, including the junctions with Josephson energies E_J , $4E_J$, and αE_J , where $\alpha = 0.72$, forming the persistent current qubit. The PCQB's transition frequency ν_{QB} is controlled during the experiments by magnetic flux threading the PCQB loop, which is the sum of a constant magnetic flux Φ_{ext} , generated by a solenoid, and a time-varying flux $\Phi(t)$, induced by a current $I(t)$ through an on-chip control line coupled to the qubit by a mutual inductance. We control the qubit using quasi-dc control pulses to tune its resonant frequency and rf pulses for qubit rotations to implement the operations, similar to Refs. 4 and 19. The operating point is set to $\Phi_{\text{ext}} = 3\Phi_0/2 + \delta\Phi_{\text{ext}}$, where $\Phi_0 = h/(2e)$ is the superconducting flux quantum and $\delta\Phi_{\text{ext}} \ll \Phi_0$. At this bias two macroscopically distinct current states exist, corresponding to a persistent current $I_p \approx \pm 300$ nA, circulating clockwise or counterclockwise. The magnetic energy of these two states corresponds to a frequency of $\epsilon(t) = \pm I_p(\Phi(t) + \delta\Phi_{\text{ext}})/h$. The Josephson junction parameters generate a tunnel matrix element between the two states of $\Delta = 3.2$ GHz. The PCQB Hamiltonian takes the form

$$H_{\text{QB}} = h(\Delta\sigma_{x,\text{QB}} + \epsilon(t)\sigma_{z,\text{QB}})/2, \quad (1)$$

where $\sigma_{x,\text{QB}}$ and $\sigma_{z,\text{QB}}$ are the normal Pauli matrices, so that the transition frequency is given by $\nu_{\text{QB}} = \sqrt{\Delta^2 + \epsilon^2(t)}$. The layout of the open-ended ($\lambda/2$) superconducting coplanar coupled stripline resonator is depicted in Fig. 1(a); the resonator resides in a galvanically isolated metallization layer on top of the

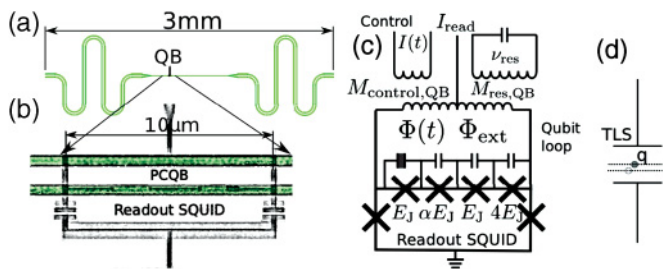


FIG. 1. (Color online) (a) Layout of the stripline resonator of total length $l_{\text{res}} = 7.1$ mm. (b) Sample micrograph (edited for clarity); isolated resonator segment in galvanically isolated top layer marked up in color (light gray). The isolation is formed by a SiO_2 layer (not visible). (c) Schematic of the qubit, the resonator, and the control. (d) A junction capacitor containing a TLS carrying a charge q tunneling between two different positions

PCQB. This resonator consists of two parallel superconducting lines supporting an odd electromagnetic mode in which currents in both lines flow in opposite directions, confining the magnetic field between the lines. Placing the PCQB's loop in the area where the magnetic field is confined creates a mutual inductance between the qubit and the resonator, coupling the zero point fluctuation current of the resonator to the PCQB's persistent current. In this paper we use the fundamental mode, a standing wave with a wavelength $\lambda = 2l_{\text{res}}$, where in the midpoint of the resonator the current flowing in the coupled striplines has a maximum, close to which the qubit is placed [Fig. 1(a)]. The schematic in Fig. 1(c) represents this resonator mode by a parallel resonant circuit formed by an inductance and capacitance. The TLS is a trapped elementary charge, tunneling between stable positions, illustrated in Fig. 1(d), and resides in the oxide layer, forming one of the qubit's junctions. Such TLSs couple to the embedding electric circuits by the electric field in dielectric junctions, thus causing an anomalous energy dispersion relation of the capacitor. The TLS and resonator are coupled very weakly electrically directly, and in our case, they are far detuned in frequency. However, either system interacts strongly with the PCQB when in resonance.

III. SPECTROSCOPY

A simple way to probe for the energy-level structure of the total system is to let the system relax to its thermodynamic ground state by keeping $I = 0$ for some time τ_{relax} . After this time the system has relaxed to its thermodynamic equilibrium state, governed by the qubit energy $h\nu_{\text{QB}}$ and effective electronic qubit temperature of 130 mK, corresponding to an excited state population of the qubit of $\sim 5\%$, subsequently ignored in the discussion. After this we apply a long ac pulse $I(t) = I_{\text{rf}} \cos(2\pi\nu_{\text{rf}}t)$ with small amplitude. I_{rf} is applied to the control line and subsequently readout of the qubit by a measurement dc superconduction quantum interference device (SQUID); we repeat this sequence N_{meas} times and record the switching events to estimate the qubit excitation probability.

The result is shown in Fig. 2, as a function of $\delta\Phi_{\text{ext}}$ and ν_{rf} , where the frequency was swept for each magnetic field to acquire the spectrum of the qubit. While the dispersion relation on the coarse scale fits the qubit dispersion relation, the insets show avoided crossings at the microscopic TLS

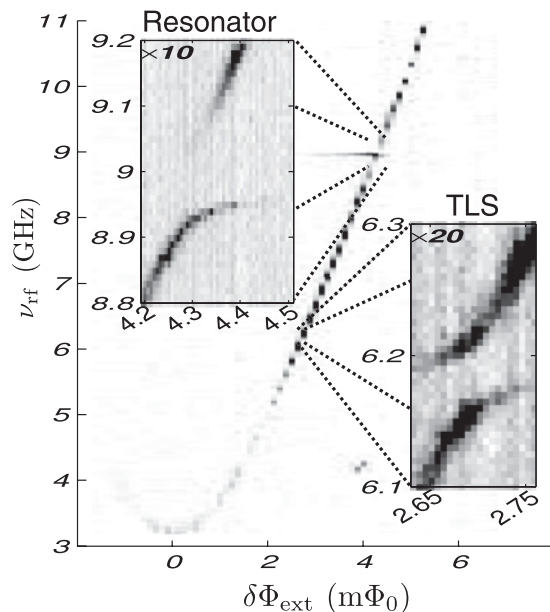


FIG. 2. Spectrum of the qubit (density) showing the population of the qubits excited state as a function of field and frequency. Insets: Higher resolution, enlarged around the anticrossings.

transition frequency $\nu_{\text{TLS}} = 6.17$ GHz and the resonator's fundamental frequency $\nu_{\text{res}} = 8.97$ GHz. The splitting of the avoided crossing at ν_{res} is $2\nu_{\text{res,QB}} = 112$ MHz (corresponding to a coupling strength $g_{\text{res,QB}} = 157$ MHz in the canonical base of the qubit). The TLS is presumably contained in a Josephson junction barrier, indicated in Fig. 1(b). The coupling of a charged TLS and a persistent current qubit was described in Ref. 16, where the maximum possible coupling strength was found to be $g_{\text{TLS,QB}} = \Delta\phi_m d/t$, where ϕ_m is the phase difference associated with the persistent current states, which is on the order of unity, $t \approx 0.6$ nm is the oxide layer thickness, and $d \approx 0.03$ nm is the distance between the stable locations, so $g_{\text{TLS,QB}} \leq 200$ MHz. The experimentally observed splitting at ν_{TLS} is $2\nu_{\text{TLS,QB}} = 54$ MHz, corresponding to a coupling strength of $g_{\text{TLS,QB}} = 55$ MHz in the qubit's canonical base. The TLS frequency ν_{TLS} fluctuated between the acquisition of the spectrum in Fig. 2 and the experiments described below, which we attribute to a fluctuation of the surrounding electric field.¹⁵ The system's total Hamiltonian in the qubit and TLS eigenbase is approximated by

$$\begin{aligned}
 H_{\text{total}} = & h\frac{1}{2}\nu_{\text{QB}}(t)\sigma_{z,\text{QB}} \\
 & + h\frac{1}{2}\nu_{\text{TLS}}\sigma_{z,\text{TLS}} \\
 & + h\nu_{\text{TLS,QB}}\sigma_{x,\text{QB}} \otimes \sigma_{x,\text{TLS}} \\
 & + h\nu_{\text{res}}(a^\dagger a + \frac{1}{2}) \\
 & + h\nu_{\text{res,QB}}(\sigma_{+,\text{QBA}} + \sigma_{-,\text{QBA}}^\dagger). \quad (2)
 \end{aligned}$$

IV. MEMORY AND ENTANGLEMENT EXPERIMENTS

During the time-domain experiments a constant external magnetic flux $\delta\Phi_{\text{ext}} \approx 4$ m Φ_0 is applied, corresponding to $\nu_{\text{QB}} = 7.92$ GHz. The system is then in the $|0,0,0\rangle$ state, where

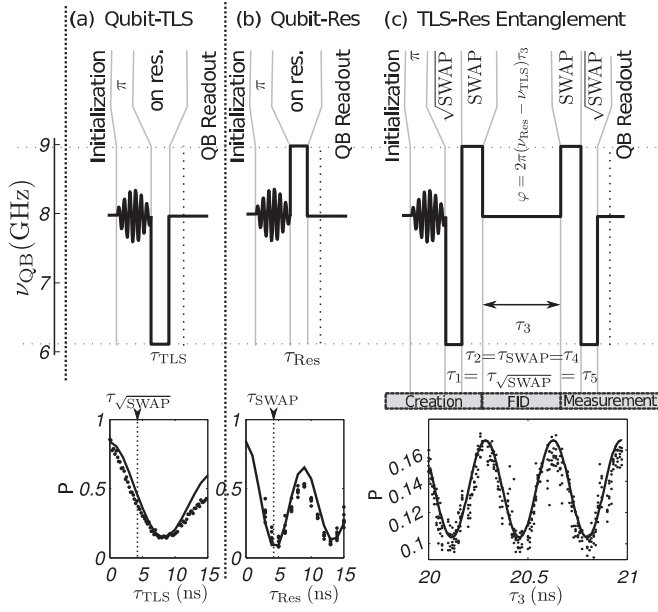


FIG. 3. (a) Pulse sequence probing the coherent resonant interaction of the qubit and the TLS for a time τ_{TLS} . Bottom: Measured qubit population (dots) and simulation result (line) (see Table I). The time required for a $\sqrt{\text{SWAP}}$ operation is indicated. (b) Pulse sequence probing the coherent resonant interaction of the qubit with the TLS for a time τ_{res} . Bottom: Measured qubit population (dots) and the simulation result (line). The time required for a SWAP operation is indicated. (c) Pulse sequence for entanglement generation, phase evolution for a time τ_3 , and projecting the entangled state to the qubit state. Bottom: Measured qubit population (dots) and fit (line) of a cosine, with the offset, phase, frequency, and amplitude as free parameters.

the first subspace denotes the PCQB state, the second denotes the TLS state, and the third denotes the resonator state. Each of the sequences depicted in Figs. 3(a)–3(c) begins with a qubit spin flip by a resonant π pulse with a duration $\tau_0 \approx 4$ ns and with an amplitude determined in a Rabi experiment, preparing the system in the $|1,0,0\rangle$ state. The input current applied to the on-chip control line is defined by a piecewise function by the pulse lengths τ_i and the quasi-dc pulse heights $I_{\text{dc},i}$, corresponding to a qubit transition frequency $\nu_{\text{QB},i}$. We represent the pulse sequences as shown in Figs. 3(a)–3(c) and model the system by H_{total} . We first characterize the qubit-TLS interaction as shown in Fig. 3(a) by bringing the excited qubit on resonance for a time τ_{TLS} , allowing us to determine $\nu_{\text{TLS,QB}}$ and the time $\tau_{\sqrt{\text{SWAP}}} = 1/(8\nu_{\text{TLS,QB}})$ needed for performing a $\sqrt{\text{swap}}$ operation. After this operation the TLS and the qubit are in the entangled Bell- $\Phi_{\text{QB,TLS}}^+$ state $(|1,0,0\rangle + |0,1,0\rangle)/\sqrt{2}$. The qubit-resonator interaction is characterized equivalently in Fig. 3(b) and the time $\tau_{\text{swap}} = 1/(4\nu_{\text{res,QB}})$ corresponding to a swap operation is determined, in which the qubit state and the single-photon state are exchanged, making the state $|0,0,1\rangle$. The combination of these two operations yields the pulse sequence in Fig. 3(c). The first quasi-dc pulse tunes the qubit in resonance with the TLS for a time $\tau_1 = \tau_{\sqrt{\text{swap}}}$ and generates the entanglement. The second to the fourth pulses form a memory sequence, during which the qubit excitation is stored in the single photon state

of the resonator, and retrieved after some storage time. The second pulse brings the qubit in resonance with the resonator for a time $\tau_2 = \tau_{\text{swap}}$, transferring the Bell state between the qubit and the TLS to a Bell state between the TLS and the resonator, $(|0,1,0\rangle + |0,0,1\rangle)/\sqrt{2}$. After this the qubit is taken off resonance for the storage time τ_3 . During this period the $(|0,1,0\rangle + |0,0,1\rangle)/\sqrt{2}$ state evolves according to a multispin Zeeman Hamiltonian as $[(|0,1,0\rangle + \exp(i\varphi)|0,0,1\rangle)]/\sqrt{2}$, where $\varphi = 2\pi\tau_3(\nu_{\text{res}} - \nu_{\text{TLS}})$. As a result, the occupation oscillates between $(|0,1,0\rangle + |0,0,1\rangle)/\sqrt{2}$ and $(|0,1,0\rangle - |0,0,1\rangle)/\sqrt{2}$, so varying the storage time τ_3 probes this coherent phase evolution. Bringing the qubit and the resonator in resonance for a time $\tau_4 = \tau_{\text{swap}}$ swaps the resonator state back to the qubit. The last pulse brings the qubit on resonance with the TLS for $\tau_5 = \tau_{\sqrt{\text{swap}}}$, generating another $\sqrt{\text{swap}}$ operation and projecting the entangled states into a measurable qubit excitation $\cos(\varphi)|1,0,0\rangle + \sin(\varphi)|0,1,0\rangle$. We plot the measured excitation probability in Fig. 3(c) as a function of τ_3 between 20 and 21 ns. Fitting using a robust least-squares method yields a frequency of $2.935 \text{ GHz} \pm 22 \text{ MHz}$, which matches the frequency difference between the TLS and the resonator.

V. DECOHERENCE IN THE SYSTEM

In order to gather information about the sample we performed a number of experimental sequences to determine its parameters. We manually fitted the data by adjusting simulation parameters of a numerical simulation to time-domain experiments.

A. Numerical simulation

The simulation is carried out using the quantum optics toolbox²³ for MATLABTM. We truncate the Hamiltonian of the harmonic oscillator to the three lowest levels (for all sequences presented here, a truncation to only two levels did not change the simulation outcome significantly). The Hamiltonian H_{total} is represented in the rotating frame and used to formulate a Lindblad-type master equation

$$\frac{\partial \rho}{\partial t} = -i/h[H_{\text{total}}(t), \rho] + \sum_i \left(C_i \rho C_i^\dagger - \frac{1}{2} C_i^\dagger C_i \rho - \frac{1}{2} \rho C_i C_i^\dagger \right), \quad (3)$$

where the C_i are the collapse operators, corresponding to decoherence channels, describing the dephasing and relaxation of the system.²⁴ We assume that the corresponding processes can be described using effective values for each subsystem and use the following $C_i \gamma_{\phi, \text{QB}}, \gamma_{\phi, \text{TLS}}$:

$$\begin{aligned} C_1 &= \sqrt{\gamma_{\text{res}} \sqrt{n_{\text{res}}}} a, \\ C_2 &= \sqrt{\gamma_{\text{res}} \sqrt{1 + n_{\text{res}}}} a^\dagger, \\ C_3 &= \sqrt{\gamma_{\text{TLS}} \sqrt{n_{\text{TLS}}}} \sigma_{+, \text{TLS}}, \\ C_4 &= \sqrt{\gamma_{\text{TLS}} \sqrt{1 + n_{\text{TLS}}}} \sigma_{-, \text{TLS}}, \\ C_5 &= \sqrt{\gamma_{\text{QB}} \sqrt{n_{\text{QB}}}} \sigma_{+, \text{QB}}, \\ C_6 &= \sqrt{\gamma_{\text{QB}} \sqrt{1 + n_{\text{QB}}}} \sigma_{-, \text{QB}}, \end{aligned}$$

TABLE I. Parameter values used in the simulation.

Parameter	Value	Meaning (Experiments used to estimate)
T_{QB}	130 mK	Initial population
T_{res}	30 mK	HO temperature
T_{TLS}	30 mK	TLS temperature
$\tau_{1,\text{QB}}$	130 ns	Qubit relaxation time
$\tau_{2,\text{QB}}$	20 ns	Qubit dephasing time
$\tau_{1,\text{TLS}}$	407 ns	TLS relaxation time
$\tau_{2,\text{TLS}}$	160 ns	TLS dephasing time
$\tau_{1,\text{HO}}$	37 ns	Resonator relaxation time
$\delta\nu_{\text{QB}}$	17 MHz	Gaussian dc frequency fluctuation

$$C_7 = \frac{\sqrt{\gamma_{\phi,\text{QB}}}}{2} \sigma_{z,\text{QB}},$$

$$C_8 = \frac{\sqrt{\gamma_{\phi,\text{TLS}}}}{2} \sigma_{z,\text{TLS}}, \quad (4)$$

where the thermal occupation number of system X n_X describes the white-noise terms to which each subsystem is exposed. We formulate these in terms of effective temperatures

$$n_X = 1 \left| \left[\exp\left(\frac{h\nu_X}{T_X k_B}\right) - 1 \right] \right|. \quad (5)$$

Low-frequency noise (quasi-dc) is taken into account by integrating the final density matrices over a normal distribution of qubit frequency offsets. Full Monte Carlo simulations brought similar results at a higher computational cost. Thus the simulation takes into account white noise and zero frequency noise. The effect of this is that the measurement of the qubit excitation probability as a function of the echo shift pulse position at fixed Ramsey times does not match the simulations, because in this sequence the neglected part of the noise spectrum plays a role.

B. Determination of the qubit dephasing

We determine the qubit parameters listed in Table I using the data in Fig. 4. We calibrate the experimental amplitude of the rf drive by adjusting the Rabi precession frequency,

perform a relaxation measurement after a π pulse, and vary the waiting time until we readout the qubit state, determining it by the qubit relaxation time. To determine the dephasing we use a Ramsey and an echo sequence. The pure dephasing time due to white noise of the qubit is determined from the echo sequence in Fig. 4 and a standard deviation a static dc noise determined by the Ramsey data in Fig. 4.

We use two memory sequences shown in Fig. 5 to determine the frequency and dephasing rates in Table I. The entanglement of the qubit and the TLS (Fig. 4) did not bring additional information, but matches the simulation, and the dephasing is mainly subject to the dephasing of the qubit.

VI. DECOHERENCE OF THE ENTANGLED STATE

The experiment consists of three parts, indicated in Fig. 3(c) by a gray shaded timeline, namely, creation, free induction decay (FID), and measurement. It is possible to probe the decoherence of the entangled state during the FID, where it is supposedly decoupled from the qubit. In Fig. 6 we show the qubit excitation probability over τ_3 ranging from 20 ns (limited by a reflection in the control line) to 60 ns in steps of 100 ps. For comparison, the results of Ramsey characterizations of the memory sequences on TLSs and resonators are shown.

A. Evaluation of the data by fitting to an analytic model

Since we disregard the first 20 ns of the data, the qubit is already decohered, and represents a background population, relaxing in time (however, not significantly, due to the qubit's relaxation time of 130 ns). Thus, the probability can be fitted by a decaying oscillation on top of the relaxation of the corresponding states by $P = A_0 \sin(\omega_0 t + \phi_0) \exp(-\gamma^* t) + A_1 \exp(-\gamma t) + P_0$. Fitting (lines in Fig. 6) the data to an exponential decay of the oscillation yields a resonator frequency of $\nu_{\text{res}} = 8.976 \text{ GHz} \pm 1 \text{ MHz}$ (95% confidence interval), a TLS transition frequency of $\nu_{\text{TLS}} = 6.060 \text{ GHz} \pm 1 \text{ MHz}$ (95% confidence interval), and an entangled state oscillation frequency of $\nu = 2.916 \text{ GHz} \pm 3 \text{ MHz}$ (standard deviation of several data sets, between which the parameters fluctuated), fulfilling the relation $\nu_{\text{res}} - \nu_{\text{TLS}} = \nu$ to a precision

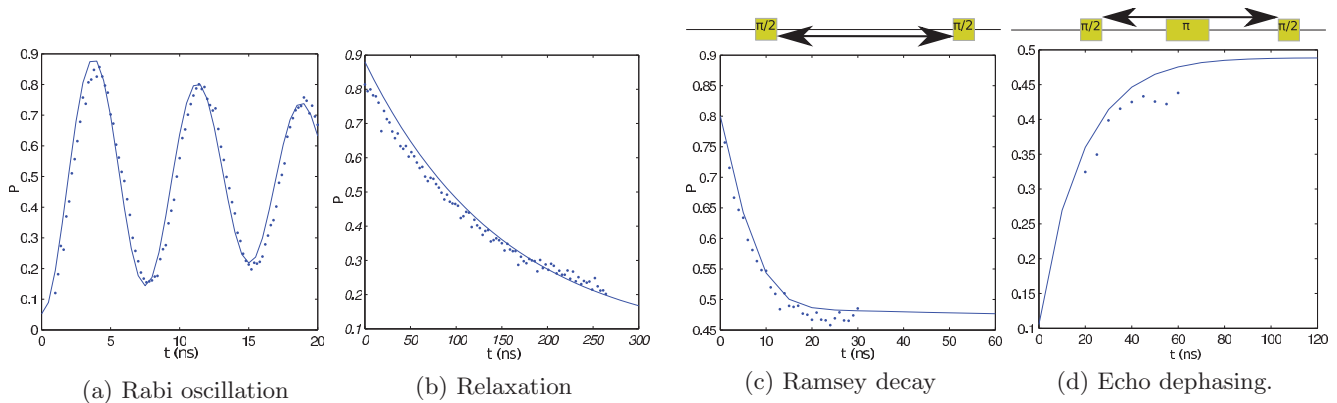


FIG. 4. (Color online) Measurements of qubit excitation probability (dots), and comparison to simulated data (line). (a) Rabi oscillation to calibrate power. (b) Relaxation after a π pulse. (c) Ramsey dephasing, mainly due to low-frequency fluctuations. The simulation assumed a white-noise spectrum, added to a fluctuating dc offset, which was adjusted by this measurement. (d) Echo decay caused by high-frequency noise.

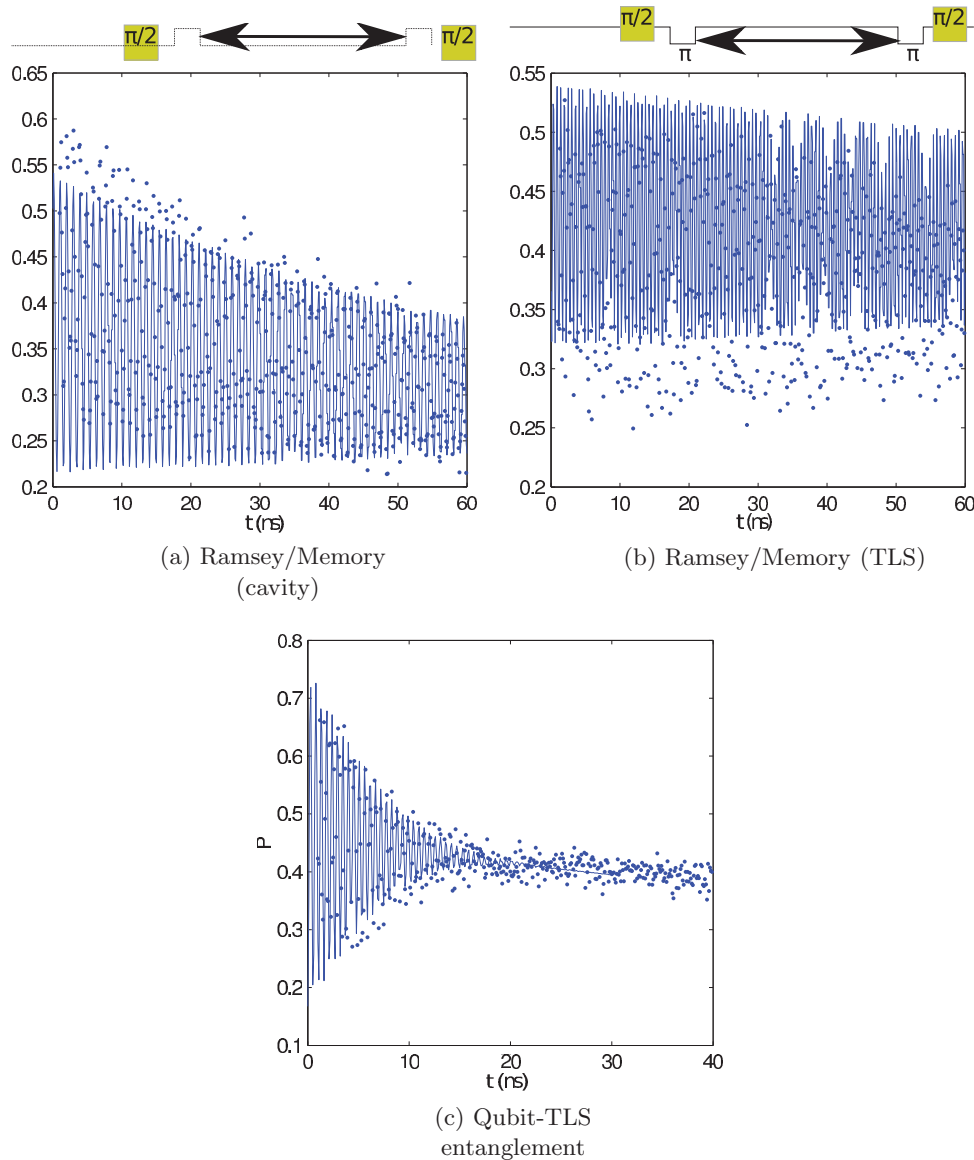


FIG. 5. (Color online) Measurements of qubit excitation probability (dots), and comparison to simulated data (line). (a) Using the cavity as a quantum memory. (b) Using the TLS as a quantum memory. (c) Entangling the qubit and the TLS.

of better than 10 MHz. The fits also yield the decay times and amplitudes A_0 at $\tau_3 = 0$ for each of the coherent signals. Each of these oscillation amplitudes is a measurement of the absolute value of the corresponding off-diagonal element in the density matrix, but affected by the efficiency η of the measurement gate. Regardless of the numerical value of this factor, any finite oscillation amplitude corresponds to a finite entanglement. In numerical simulations taking into account experimental pulse-shaping limitations, we estimate $\eta \approx 0.6$, yielding a concurrence for $A_0 = 0.13$ at $\tau_3 = 0$ (extrapolated) of $C = A_0/\eta = 0.2$. We compare the decay rates in the systems; the echo and Ramsey dephasing times of the qubit are 13.6 and 6.3 ns.

B. Determining the type of noise acting on the TLS

For estimating the entangled states coherence properties we use five data sets (we ignore one additional data set as an

outlier, which was most likely affected by a setup instability), acquired directly successive to each other. This was to resolve the comparatively low visibility signal and isolate effects of a slow fluctuating ϕ_0 due to setup stability and ω_0 due to changes of the TLS environment from a real decoherence source on the time scale of the experiment. When fitting each of the five data sets we find $\gamma^* = 38.8 \pm 3.1$ ns. Then, instead fitting to the average over the five data sets, we find a γ^* of 28 ns. This indicates that a low-frequency fluctuation of ω_0 is indeed present. Since the resonator frequency can be considered stable, this fluctuation must be attributed to the TLS.

This has to be compared to the predicted entangled state's decay of 40.8 ± 14.4 ns (90% confidence interval). The latter value is calculated from the memory dephasing times 76 ± 20.7 ns (95% confidence interval) for the resonator and 89 ± 39 ns (95% confidence interval) for the TLS. All of these times include the relaxation-induced dephasing rates and the

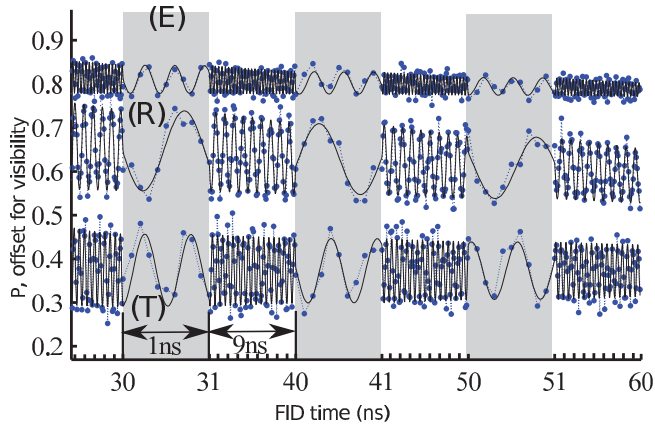


FIG. 6. (Color online) Coherent oscillation of the qubit excitation acquired by Ramsey memory sequences (Resonator: $\tau_1 = \tau_5 = 0$; TLS: $\tau_2 = \tau_4 = 0, \tau_1 = \tau_5 = \tau_{\text{swap}}$) on the TLS (T) and the resonator (R), and the entanglement sequence (E) in Fig. 2 as a function of the storage time τ_3 . The lines indicate the fits from which the data are extracted; these fits are fits to an exponentially decaying background and a coherent oscillation. At the three times the horizontal scale of the figure was stretched for better visibility of the agreement between fits (solid line) and experimental data (dots, dotted line).

pure dephasing rates; a superoperator calculation shows that these can be added, also for the decay rate of the entangled state. From the numbers above, the most likely rate for an additional decoherence channel is 1/791 ns, with an upper bound (95% confidence interval) of 1/80 ns using the data presented.

VII. SUMMARY

To conclude, we have shown an extremely heterogeneous quantum experiment consisting of three effective qubits, in which a PCQB acts as a transformer between a stripline resonator and a microscopic TLS inside one of the qubit Josephson junctions. We use this qubit to generate, mediate, and measure entanglement between the two other systems. The frequency of the entangled state matches the predicted relations exactly, and the amplitude, equivalent to the concurrence, decays over a time scale predicted from the resonator and TLS dephasing, and is significantly longer than the qubit's dephasing time. The additional decoherence rate besides the decoherence of the entangled subsystems during the time of free induction decay is estimated to be at least one order of magnitude times lower than the qubit dephasing rate. This verifies that the qubit itself acts mainly as a mediator and participates after the entanglement creation only weakly in the entangled state dynamics, and demonstrates that the coherence time of a single active element, used as a mediator to generate entanglement between passive quantum systems otherwise isolated from the environment, does not limit the decoherence times of the mediated entangled states directly.

ACKNOWLEDGMENTS

We thank to K. Kakuyanagi, F. Deppe, H. Yamaguchi, Y. Tokura, and X. B. Zhu for technical help and valuable comments. This work was supported in part by Funding Program for World-Leading Innovative R&D on Science and Technology (FIRST), Scientific Research of Specially Promoted Research No. 18001002 by MEXT, and Grant-in-Aid for Scientific Research (A) No. 22241025 by JSPS.

*work@alexanderkemp.name

†semba@will.brl.ntt.co.jp

¹J. Clarke and F. K. Wilhelm, *Nature (London)* **453**, 1031 (2008).

²A. Wallraff, D. I. Schuster, A. Blais, L. Frunzio, R.-S. Huang, J. Majer, S. Kumar, S. M. Girvin, and R. J. Schoelkopf, *Nature (London)* **431**, 162 (2004).

³I. Chiorescu, P. Bertet, K. Semba, Y. Nakamura, C. J. P. M. Harmans, and J. E. Mooij, *Nature (London)* **431**, 159 (2004).

⁴J. Johansson, S. Saito, T. Meno, H. Nakano, M. Ueda, K. Semba, and H. Takayanagi, *Phys. Rev. Lett.* **96**, 127006 (2006).

⁵J. Majer, J. M. Chow, J. M. Gambetta, J. Koch, B. R. Johnson, J. A. Schreier, L. Frunzio, D. I. Schuster, A. A. Houck, A. Wallraff, A. Blais, M. H. Devoret, S. M. Girvin, and R. J. Schoelkopf, *Nature (London)* **449**, 443 (2007).

⁶M. A. Sillanpaa, J. I. Park, and R. W. Simmonds, *Nature (London)* **449**, 438 (2007).

⁷A. Blais, R.-S. Huang, A. Wallraff, S. M. Girvin, and R. J. Schoelkopf, *Phys. Rev. A* **69**, 062320 (2004).

⁸T. P. Spiller, K. Nemoto, S. L. Braunstein, W. J. Munro, P. van Loock, and G. J. Milburn, *New J. Phys.* **8**, 30 (2006).

⁹H. J. Kimble, *Nature (London)* **453**, 1023 (2008).

¹⁰L. DiCarlo, J. M. Chow, J. M. Gambetta, L. S. Bishop, B. R. Johnson, D. I. Schuster, J. Majer, A. Blais, L. Frunzio, S. M. Girvin, and R. J. Schoelkopf, *Nature (London)* **460**, 240 (2009).

¹¹M. Ansmann, H. Wang, R. C. Bialczak, M. Hofheinz, E. Lucero, M. Neeley, A. D. O'Connell, D. Sank, M. Weides, J. Wenner, A. N. Cleland, and J. M. Martinis, *Nature (London)* **461**, 504 (2009).

¹²R. W. Simmonds, K. M. Lang, D. A. Hite, S. Nam, D. P. Pappas, and J. M. Martinis, *Phys. Rev. Lett.* **93**, 077003 (2004).

¹³P. Bertet, I. Chiorescu, G. Burkard, K. Semba, C. J. P. M. Harmans, D. P. DiVincenzo, and J. E. Mooij, *Phys. Rev. Lett.* **95**, 257002 (2005).

¹⁴J. Lisenfeld, C. Müller, J. H. Cole, P. Bushev, A. Lukashenko, A. Shnirman, and A. V. Ustinov, *Phys. Rev. B* **81**, 100511 (2010).

¹⁵Z. Kim, V. Zaretsky, Y. Yoon, J. F. Schneiderman, M. D. Shaw, P. M. Echternach, F. C. Wellstood, and B. S. Palmer, *Phys. Rev. B* **78**, 144506 (2008).

¹⁶A. Lupascu, P. Bertet, E. F. C. Driessen, C. J. P. M. Harmans, and J. E. Mooij, *Phys. Rev. B* **80**, 172506 (2009).

¹⁷R. Simmonds, M. Allman, F. Altomare, K. Cicak, K. Osborn, J. Park, M. Sillanp, A. Sirois, J. Strong, and J. Whittaker, *Quant. Info. Process.* **8**, 117 (2009).

¹⁸A. M. Zagoskin, S. Ashhab, J. R. Johansson, and F. Nori, *Phys. Rev. Lett.* **97**, 077001 (2006).

¹⁹M. Neeley, M. Ansmann, R. C. Bialczak, M. Hofheinz, N. Katz, E. Lucero, A. O'Connell, H. Wang, A. N. Cleland, and J. M. Martinis, *Nat. Phys.* **4**, 523 (2008).

²⁰See Supplemental Material at <http://link.aps.org/supplemental/10.1103/PhysRevB.84.104505> for technical details.

²¹J. E. Mooij, T. Orlando, L. Levitov, L. Tian, C. H. van der Wal, and S. Lloyd, *Science* **285**, 1036 (1999).

²²P. Bertet, I. Chiorescu, K. Semba, C. J. P. M. Harmans, and

J. E. Mooij, *Phys. Rev. B* **70**, 100501 (2004).

²³Sze M Tan, *J. Opt. B: Quantum and Semiclassical Optics* **1**, 424 (1999).

²⁴K. Mølmer, Y. Castin, and J. Dalibard, *J. Opt. Soc. Am. B* **10**, 524 (1993).